# Supplementary Information
# Combined Neural Network Potential and Density Functional Theory Study of $\mathrm{TiAl_2O_5}$ Surface Morphology and Oxygen Reduction Reaction Overpotentials

Mitchell C. Groenenboom,*,† Rachel M. Anderson,‡ James A. Wollmershauser,¶ Derek J. Horton,‡ Steven A. Policastro,‡ and John A. Keith†

†*Department of Chemical and Petroleum Engineering*
*University of Pittsburgh*
*Pittsburgh, Pennsylvania 15261, United States*
‡*Center for Corrosion Science and Engineering*
*U.S. Naval Research Laboratory*
*4555 Overlook Ave. SW, Washington, D.C. 20375, United States*
¶*Material Science & Technology Division*
*U.S. Naval Research Laboratory*
*4555 Overlook Ave. SW, Washington, D.C. 20375, United States*

E-mail: mitch.groenenboom@gmail.com

# Training and Validation of Neural Networks

We created a dataset of 1077 $TiAl_2O_5$ structures from which 850 structures were selected as an initial training set. The dataset contained the coordinates, energies, and forces of 307 equation of state structures, 352 structures with stressed and strained unit cells, 124 crystalline structures with individual Ti/Al/O atoms moved within the crystalline lattice, 127 annealed annealed surface structures, 50 annealed bulk structures, and 117 structures from surface vacancy diffusion pathways. We later added 100 amorphous surface structures to the training set. These structures were produced from crystalline surface structures that were annealed with our initial neural network as described in the main text. We calculated the energies of all structures using VASP using the parameters described in the computational methods section. Geometry optimizations were only performed on crystalline surface structures and the fully amorphous surfaces. Vacancy diffusion pathways were optimized with gSS-NEB optimizations.

All equation of state (EOS) and unit cell stress and strain calculations were single point energy calculations on structures consisted of a single $TiAl_2O_5$ unit cell containing two Ti atoms, four Al atoms, and ten O atoms. EOS structures were created by uniformly compressing or expanding the crystalline $TiAl_2O_5$ unit cell by a factor of x ($0.6 < x < 1.5$) with a higher density of structures located around $x = 1$. Stress and strain structures performed similar compressions/expansions of the unit cell in one direction at a time. All 124 structures with moved Ti, Al, or O atoms consisted of a 2x2x1 supercell of $TiAl_2O_5$ unit cells. Each structure moved a single Ti, Al, or O atom +/- 0.25 or 0.50 Å in the x-, y-, or z-direction. Annealed surfaces were obtained from high temperature (1100 K) Born-Oppenheimer molecular dynamics (BOMD) simulations on a 3x2x2 slab of $TiAl_2O_5$ unit cells that was periodic in the x- and y-direction with 20 Å of vacuum space separating slabs in the z-direction. Annealed bulk structures were obtained from high temperature BOMD simulations on a 3x2x1 supercell of $TiAl_2O_5$ unit cells that was periodic in every direction. All annealing simulations used a timestep of 1 fs. Vacancy diffusion pathways were located using gSS-NEB optimizations on a 2x3 supercell of the (010) crystalline surface that was two layers thick, and a 3x2 supercell of the (001) crystalline surface that was two layers thick. All of the surface structures produced from neural network annealing simulations originated from a 3x2 supercell of a (010) crystalline surface that was two layers thick, consisted of 144 atoms, 30 Å of vacuum space, and had 9.77 x 10.85 Å surface. All calculations used k-point grids that were inversely proportional to that used for the bulk $TiAl_2O_5$ unit cell (4 x 4 x 4) and an energy cutoff of 700 eV. All of the structures, energies, and forces are provided in a json database file in the Supporting Information.

Table S1 shows the error per atom for neural network one (NN1) and neural network two (NN2) separated into distinct subsets of the training and validation sets. The RMSE, average error, and standard deviation for the validation set is smaller than those of the training set for NN2. This indicated that NN2 was not overfit for these types of structures. NN1 was trained to only crystalline structures, and has large errors for the amorphous type structures that we later included in the training set. However, NN1 does not appear to be overfitting when comparing the validation set without the additional amorphous structures. These RMSE values are significantly larger than necessary for our neural network potentials to be chemically accurate (RMSE $<$ 5 meV/Atom) with respect to our DFT calculations. As described in the main text, we opted to train neural networks smaller neural networks with larger errors because these potentials required less computational resources than larger, more accurate neural networks. All structures generated with our neural networks were fully optimized with DFT before being modeled as oxygen reduction reaction catalysts, so the absolute accuracy of NN1 and NN2 is less important than their ability to quickly generate a wide variety of unique structures.

The error for amorphous surfaces is significantly larger than the error of the bulk crystalline structures and structures annealed with DFT (1.5-2x larger for NN2 and 3-4x larger for NN1). This is expected because our initial training set contained no amorphous surface structures. Fortunately, the addition of amorphous structures to the dataset significantly improved the ability of NN2 to model these structures (decreasing the error by more than 50%). This suggests that we could approach the same level of accuracy that was achieved for the other types of $TiAl_2O_5$ structures if we incorporated more amorphous structures into the training set.

**Table S1: NN1 and NN2 error analysis**

**NN1 Residual Error (meV/Atom)**

| | **Training Set** | | |
|---|---|---|---|
| | **All Structures** | **No Amorphous Structures** | **Only Amorphous Structures** |
| **RMSE** | 17.6 | - | - |
| **Average** | 1.3 | - | - |
| **StDev** | 17.6 | - | - |
| | **Validation Set** | | |
| | **All Structures** | **No Amorphous Structures** | **Only Amorphous Structures** |
| **RMSE** | 28.0 | 17.0 | 51.5 |
| **Average** | -8.4 | 0.4 | -41.8 |
| **StDev** | 26.7 | 16.9 | 30.0 |

**NN2 Residual Error (meV/Atom)**

| | **Training Set** | | |
|---|---|---|---|
| | **All Structures** | **No Amorphous Structures** | **Only Amorphous Structures** |
| **RMSE** | 17.2 | 16.2 | 32.2 |
| **Average** | -0.4 | 0.8 | -27.4 |
| **StDev** | 17.2 | 16.2 | 16.8 |
| | **Validation Set** | | |
| | **All Structures** | **No Amorphous Structures** | **Only Amorphous Structures** |
| **RMSE** | 15.6 | 13.6 | 19.7 |
| **Average** | -5.2 | -2.2 | -12.6 |
| **StDev** | 14.7 | 13.4 | 15.1 |

# Comparing Neural Networks with/without Amorphous Structure Training Data

We previously calculated the ORR energetics of an amorphous $TiO_2$ surface model because $TiO_2$ surfaces become amorphous after prolonged exposure to an electrolyte.[1] Performing an analogous study of $TiAl_2O_5$ required an amorphous $TiAl_2O_5$ surface model. Amorphous structures can be generated by annealing crystalline structures at high temperatures using molecular dynamics simulations.[2] Performing these simulations with DFT is extremely computationally expensive and limits the number of potential surface models that can be created. Molecular dynamics simulations could be performed with a classical or reactive forcefield, but no forcefield parameters exist for $TiAl_2O_5$. To facilitate less computationally expensive molecular dynamics simulations, we trained neural networks to $TiAl_2O_5$ data. Neural networks are more computationally expensive than classical or reactive forcefields (such as ReaxFF), but they are significantly less computationally expensive than DFT. Neural networks can also be more accurate than forcefield based approaches, and their accuracy can be continuously refined with the addition of more training data.[3]

We used NN1 to perform annealing simulations as described in the computational methods section. NN1 had significant errors when compared against the DFT energetics for both amorphous surface structures obtained from during the annealing simulation trajectory (Figure S1a) and fully quenched amorphous surface structures (Figure S1b). These deviations result from the lack of amorphous structures in our original training set.

Adding the amorphous surface structures generated with NN1 to the training set of our second neural network (NN2) dramatically improved the model's accuracy with amorphous surface structures. The energies of the training set structures and the additional surface structures obtained from a new annealing simulation carried out with NN2 agreed much better with the DFT energies of the corresponding structures (see Figure S1a). The NN2 training set points in Figure S1a are the energies of the structures in the NN1 Annealed

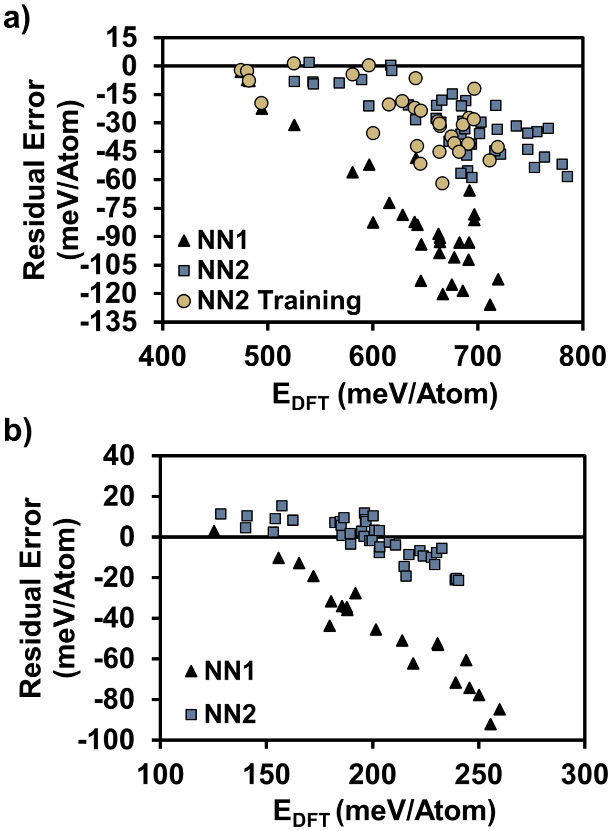

Figure S1: Parity plots of neural network (NN) and DFT absolute energies for surface structures that were a) annealed and b) annealed and quenched with neural network one (NN1) and two (NN2). The "NN1 Annealed Surf." and "NN2 Training Set" consist of the same structures but calculated with NN1 and NN2 respectively. All DFT energies were calculated with PBE.

Surfaces data set calculated with NN2. Comparing these energies shows that refitting our neural network improves the accuracy of the amorphous structures.

Fortunately, the addition of high energy amorphous surfaces to the training set also improved NN2's accuracy with fully quenched amorphous surface structures despite the absence of training data in this region of phase space (see Figure S1b). This type of training-validation feedback loop could be used to continuously improve the accuracy of neural networks for specific types of surface structures. These improvements do not degrade the ability of NN2 to model crystalline bulk and surface structures. Both NN1 and NN2 have similar error distributions for non-amorphous structures (as seen in Table S1).

Figures S2 and S3 show the errors between the neural network energies and DFT energies for different types of bulk crystalline $TiAl_2O_5$ structures computed with NN1 and NN2. Although the exact fit is different for each neural network, there is a similar overall distribution of errors. This is in agreement with the statistics shown in Table S1. Increasing the symmetry function cutoff radius or the number of symmetry functions used by our neural net potentials would likely decrease the overall error of the potentials at the cost of computational speed.

Figure S4 shows the error distribution of annealed surfaces and bulk structures for both neural net potentials. Again, the error and distribution of each neural network is similar, but the addition of amorphous structures into the training set of neural network two slightly improves the ability of the neural network to represent some annealed surfaces.

## Creating Accurate Surface Models

We created defective and amorphous surfaces by annealing crystalline surfaces with NN1 as described in the main text. Figure S5 compares the energies of these surfaces computed with NN1 and DFT. While NN1 matches the relative trend of the crystalline and defective surfaces (zones I and II), it has large errors for the amorphous surface structures. NN1 was not trained to any amorphous structural data, so this is not unexpected. The DFT energetics suggest that the amorphous surfaces found by these annealing simulations are too unstable to form at temperatures near 300 K.

Figure S6 shows the Ti/Al/O-Ti/Al/O and Ti-Ti/Al radial distribution functions (RDFs) of 4 different amorphous structures that were annealed and quenched with NN1. The structures produced by NN1 do not significantly change after being fully relaxed with DFT. While the exact height and location of the peaks shift, the general structure is preserved. These changes are most noticeable in the Ti-Ti/Al RDF. The agreement between the peaks at $r < 4$ Å shows that structures obtained with NN1 are highly similar to those that would be

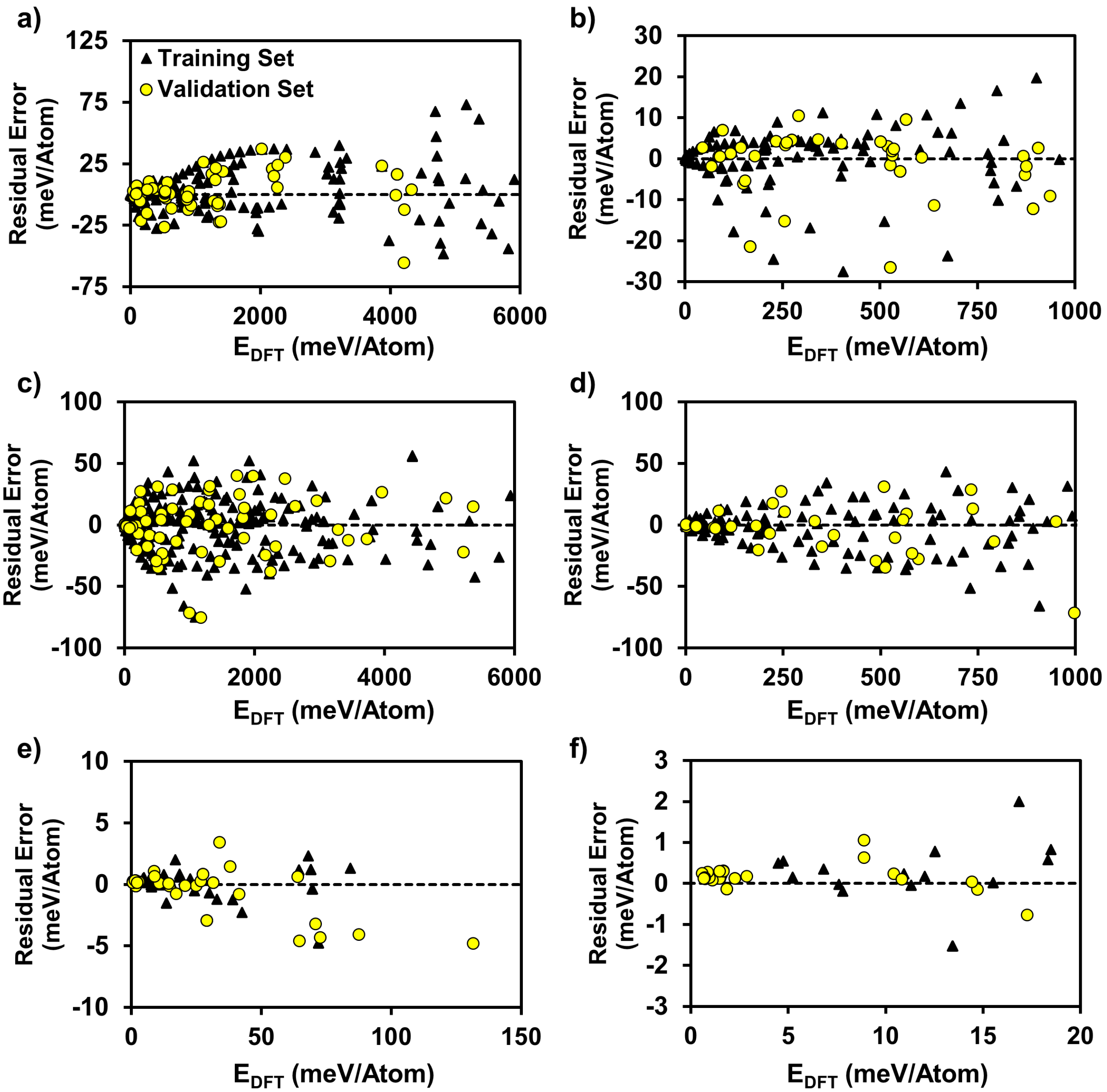

Figure S2: The error in the training and validation set for neural network one for a) and b) all equation of state data, c) and d) independent stresses on each unit cell vector, and e) and f) moving individual Ti, Al, and O atoms in the x, y, and z directions within a crystalline supercell. All energies are referenced against that of the crystalline material. Residual errors remain small relative to the overall energy of the system.

predicted by DFT. The total RDFs (Ti/Al/O-Ti/Al/O) appear similar, while the Ti-Ti/Al RDFs can be used to differentiate the amorphous surface structures. A real amorphous $TiAl_2O_5$ surface would likely have a Ti-Ti/Al RDF that is an average of many small amor-

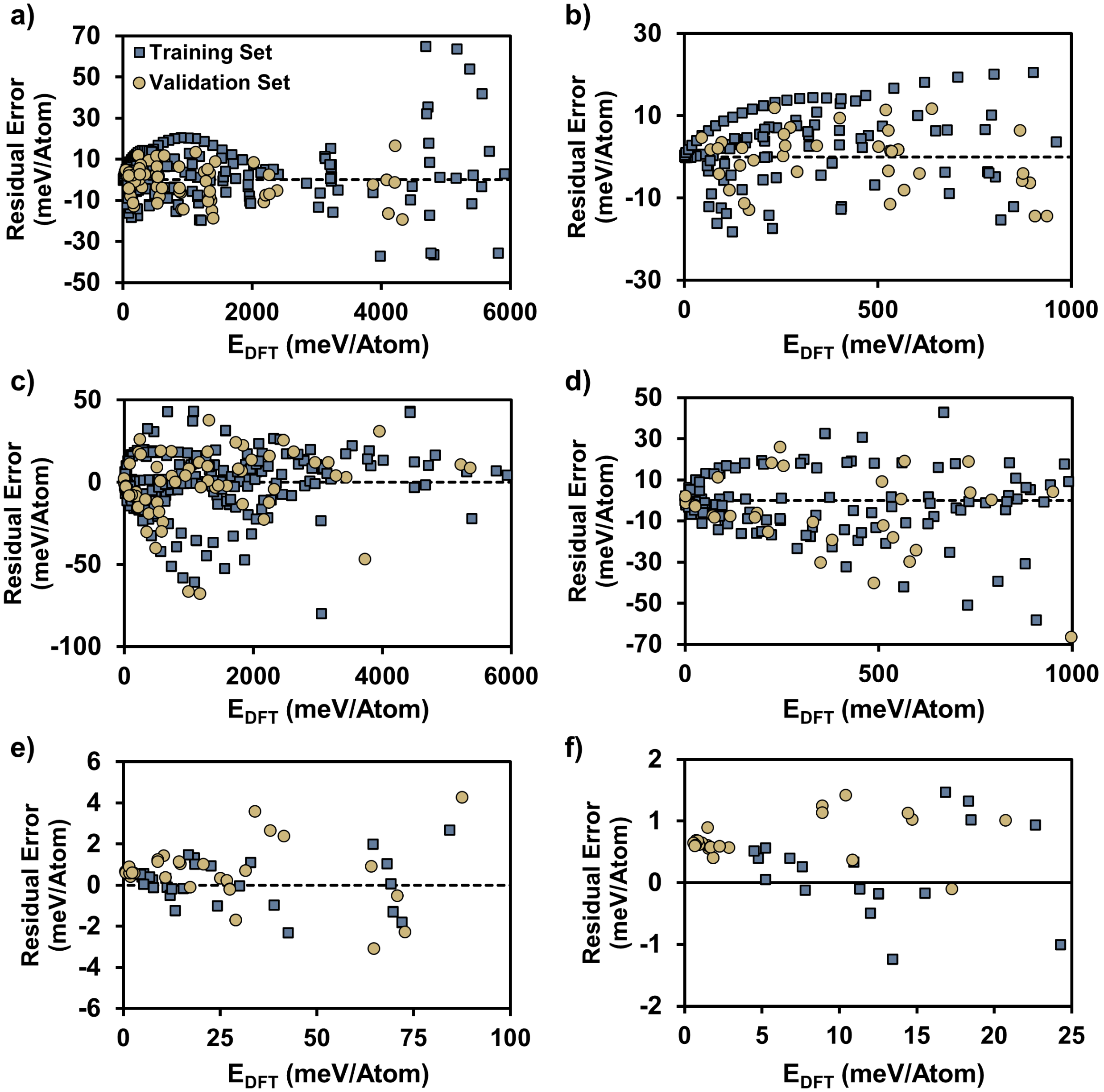

Figure S3: The error in the training and validation set for neural network two for a) and b) all equation of state data, c) and d) independent stresses on each unit cell vector, and e) and f) moving individual Ti, Al, and O atoms in the x, y, and z directions within a crystalline supercell. All energies are referenced against that of the crystalline material. Residual errors remain small relative to the overall energy of the system.

phous surface segments that are contained in our amorphous surface models.

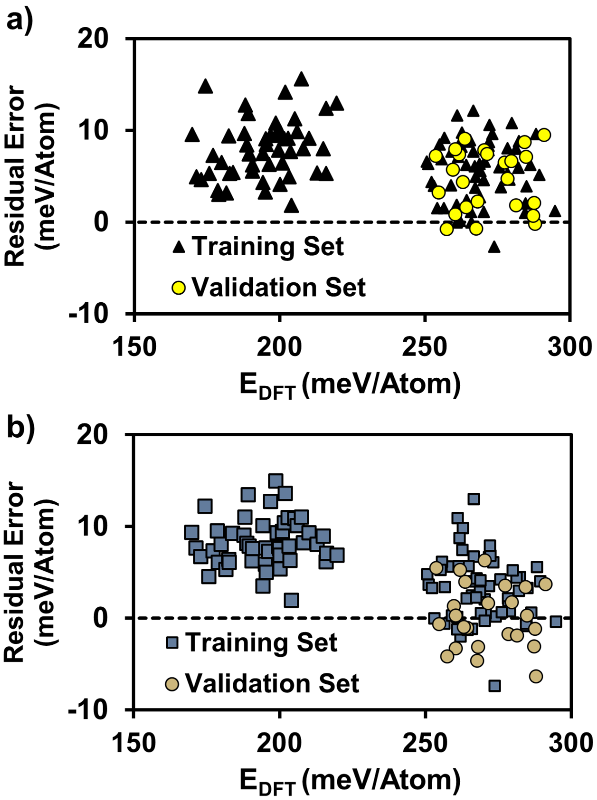

Figure S4: The error in the training and validation set for annealed bulk structures computed with a) NN1 and b) NN2. All energies are referenced against that of the crystalline material.

## Calculating ORR Overpotentials

We selected the six surface models shown in Figure S7 to characterize the atomic scale factors that affect the ORR activity of $TiAl_2O_5$ surfaces. These surfaces were selected to compare how surfaces with increasing concentrations of structural defects could affect the ORR activity of an oxide catalyst. We hypothesized that minor defects (such as the crystalline surfaces with swapped Ti/Al atoms) would have similar reactivity to the crystalline surface, while larger defects would result in activities that converged to those of the fully amorphous oxide surface.

Many multi-step electrochemical reactions can have their maximum activity limited by scaling relationships between the binding energies of reaction intermediates adsorbed to the catalyst surface. Figure S8 shows the scaling relationship between *OOH and *OH bound

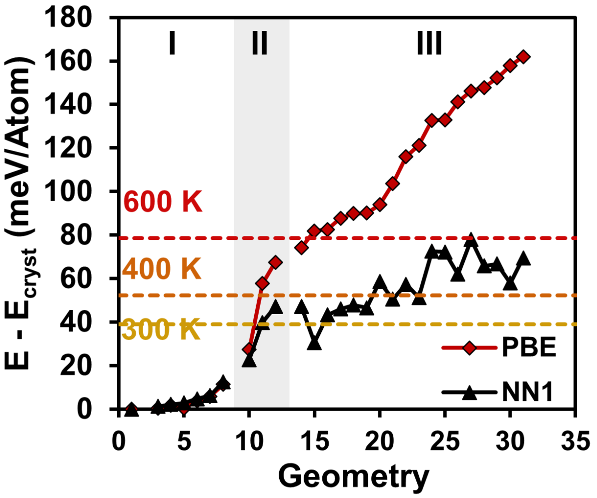

Figure S5: A comparison of neural network and DFT energies for surface structures annealed and quenched with NN1. Zone I = crystalline surfaces with swapped Ti/Al atoms, II = surface defects, III = amorphous surface structures. The 300, 400, and 600 K lines correspond to the kinetic energy present at each temperature added to the energy of the relaxed (010) crystalline surface ($E_{cryst,DFT}$ = 98.9 and $E_{cryst,NN}$ = 105.5 meV/Atom). All amorphous structures require a significant amount of energy and are unlikely to form at lower temperatures without outside influence.

to doped and undoped surface sites in our crystalline and amorphous $TiAl_2O_5$ surfaces. This correlation is responsible for estimating the left side of the activity volcano when ORR overpotentials are plotted as a function of the binding energy of *OOH to the surface. The imperfect correlation causes certain surface sites to not fall directly on the predicted activity volcano.

While crystalline surface models may only have one or two unique reaction sites, defective and amorphous surface models have a larger number of unique adsorption sites. The surfaces shown in Figure S7 have a number of unique reaction sites, and it is important to understand how ORR activity can vary on a site-by-site basis. Figure S9 shows the distributions of ORR overpotentials for each surface shown in Figure S7 as computed with HSE06. The amorphous surface (Figure S9a) and defect B (Figure S9b) have a much wider variance of activity than surfaces with fewer defects. These surfaces are predicted to have relatively similar gas and solvent phase ORR activity, while solvation corrections significantly affect the reactivity of

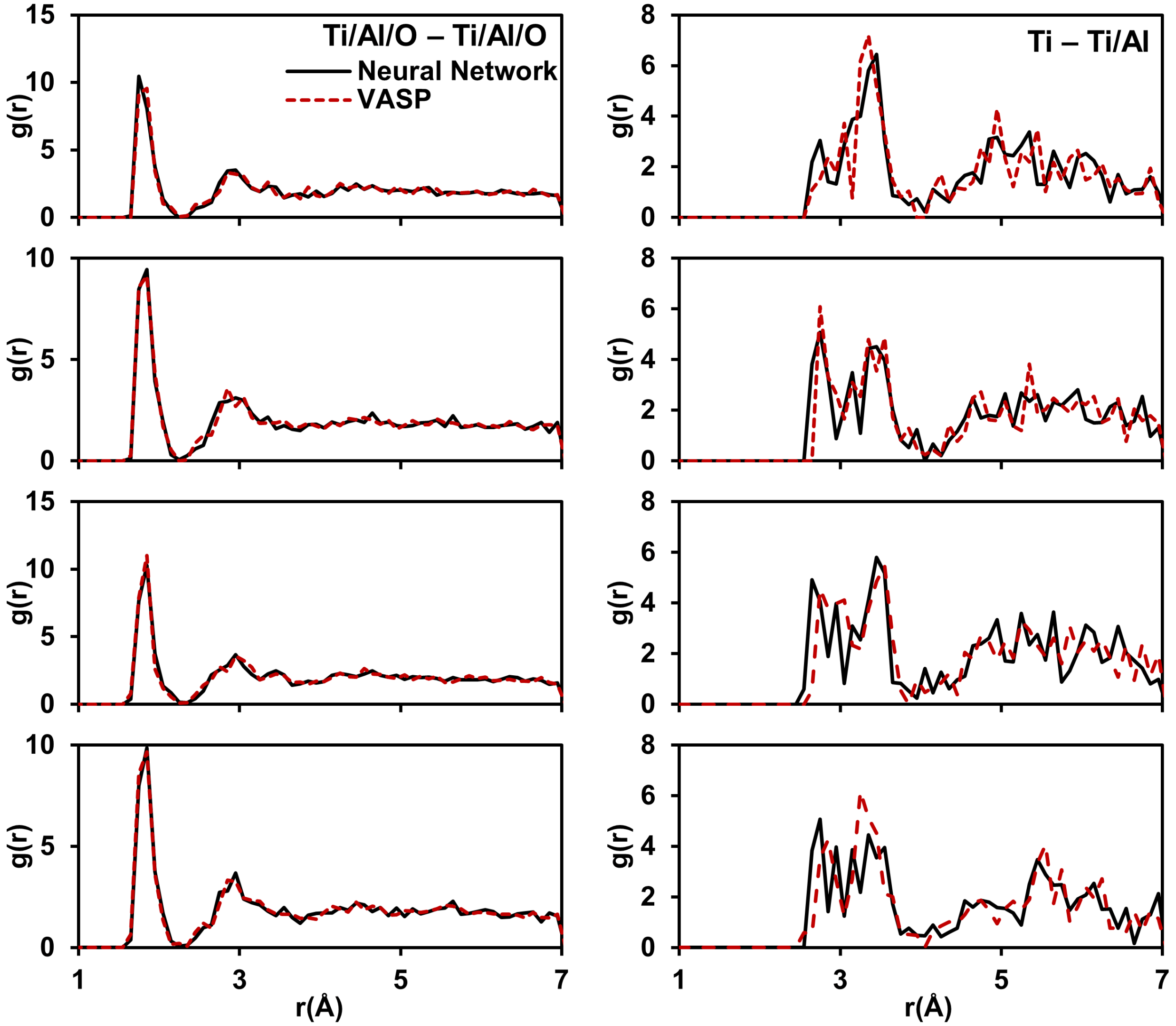

Figure S6: The Ti/Al/O-Ti/Al/O and Ti-Al/Ti RDFs for four different annealed structures. Each structure was fully relaxed with DFT (PBE) after being annealed and quenched using a neural network. The Ti-Ti/Al radial distribution function shows the variety of different structures that can be observed with annealing simulations.

the crystalline materials. As discussed in the main text, the more stable surfaces are less effective ORR catalysts. These trends are mirrored by the overpotentials of each surface predicted with PBE (see Figure S10).

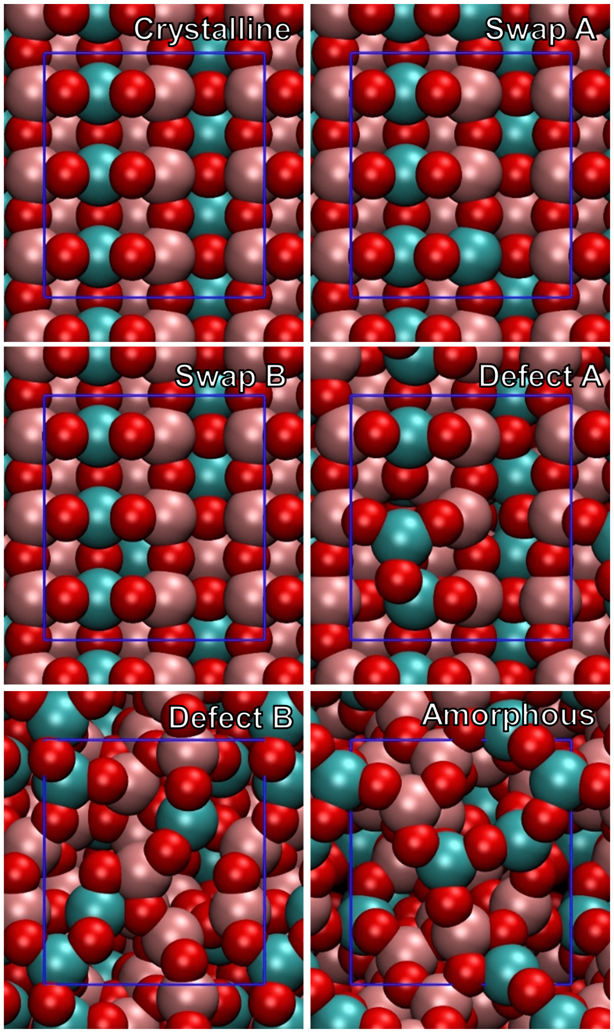

Figure S7: The low energy (010) crystalline surface, two (010) crystalline surfaces with swapped Ti/Al atoms, two defective surfaces produced by annealing simulations, and the lowest energy amorphous surface located from an annealing simulation.

# Determining Dopant Oxidation States

Accurately modeling dopants in the $TiAl_2O_5$ surface requires modeling the correct dopant oxidation state. Replacing a $Ti^{4+}$ or $Al^{3+}$ in the surface biases the dopant toward the oxidation state of the atom that it replaced. This is not always the correct oxidation state for the dopant at experimentally relevant conditions. To estimate the oxidation states of each dopant, we performed a Bader charge analysis. We estimated the oxidation state of each dopant by comparing the Bader charges of metal dopants against Bader charges of each

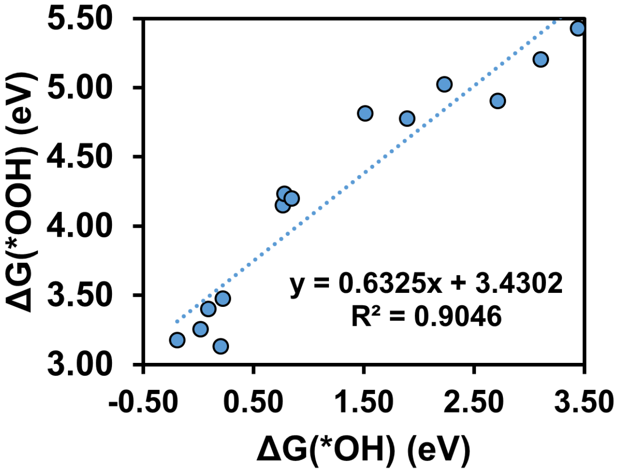

Figure S8: The scaling relationship between *OOH and *OH on the doped $TiAl_2O_5$ surfaces.

dopant in a material where their oxidation states were known. In many cases, we replaced $Ti^{4+}$ or $Al^{3+}$ with dopants that should be either 4+ or 3+ to easily achieve the desired oxidation state. Other dopants, like $Mn^{2+}$ and $Co^{2+}$, required surface modifications to reach their desired oxidation states. Table S2 shows the Bader charges of each dopant in the crystalline and amorphous surfaces. We previously used this approach to successfully model the effect of dopants incorporated into $TiO_2$.

## X-ray Photoelectron Spectroscopy

To characterize the cast alloys, X-ray diffraction (XRD) and X-ray photoelectron spectroscopy (XPS) were performed. Prior to analysis, the alloys were polished with 1 $\mu$m diamond polish and left in air for 4 days. High-resolutions scans were collected for each of the elements using a Thermo K-$\alpha$ XPS system with an Al K-$\alpha$ x-ray source and a 400 $\mu$m diameter spot size. Data analysis was performed using the CasaXPS software system. The atomic concentration of the aluminum and dopant element in the oxide was quantified and tabulated below.

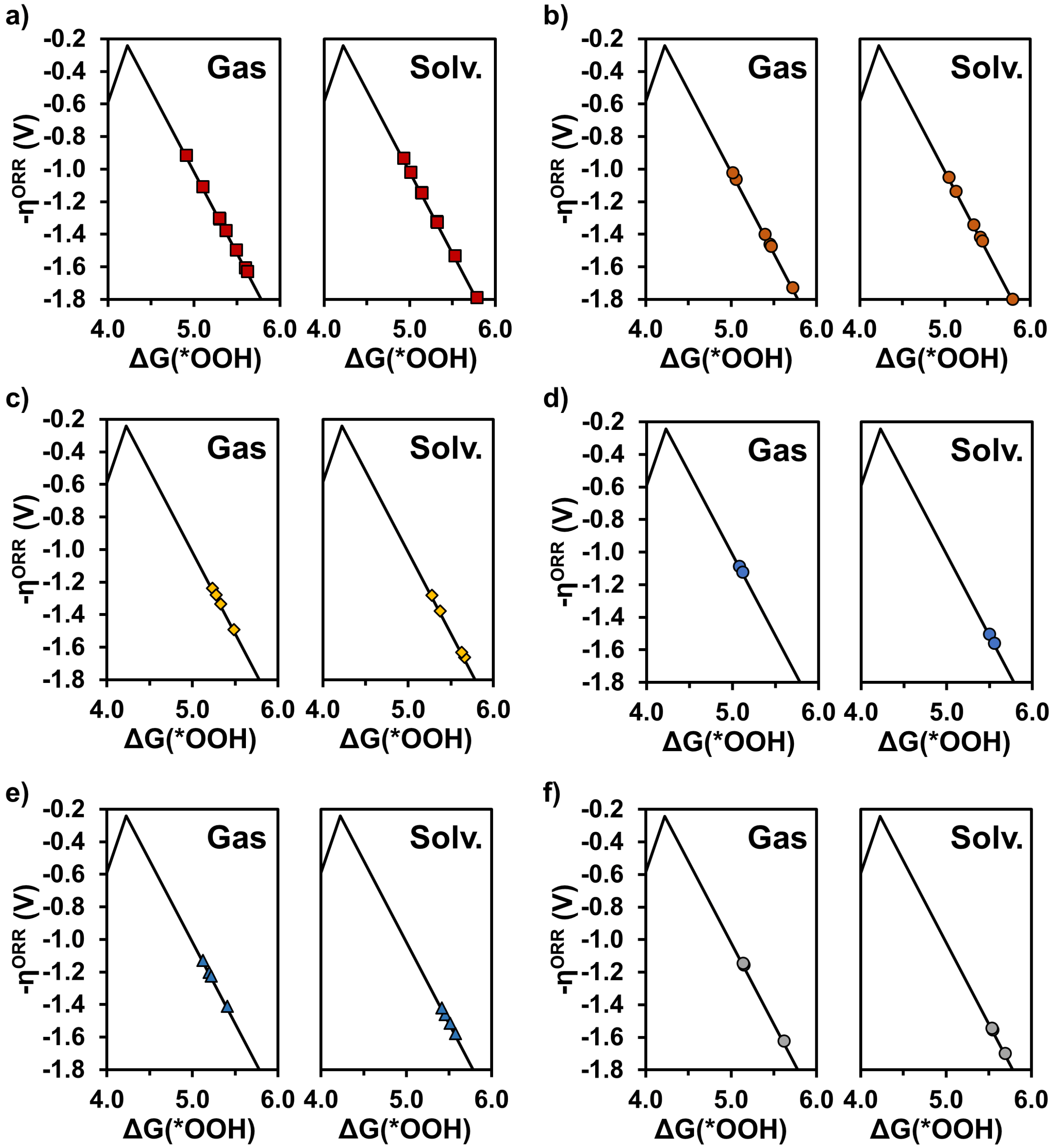

Figure S9: The ORR overpotentials for all potential reaction sites on the a) Amorphous, b) Defect B, c) Defect A, d) Swap B, e) Swap A, and f) Crystalline $TiAl_2O_5$ surfaces. All overpotentials are computed from HSE06 energy calculations on structures optimized with PBE.

# X-ray Diffraction Analysis

XRD was performed using a Cu K-$\alpha$ X-ray source to confirm the single-phase nature of the alloy. The diffraction patterns indicate that each alloy is likely a single phase, although

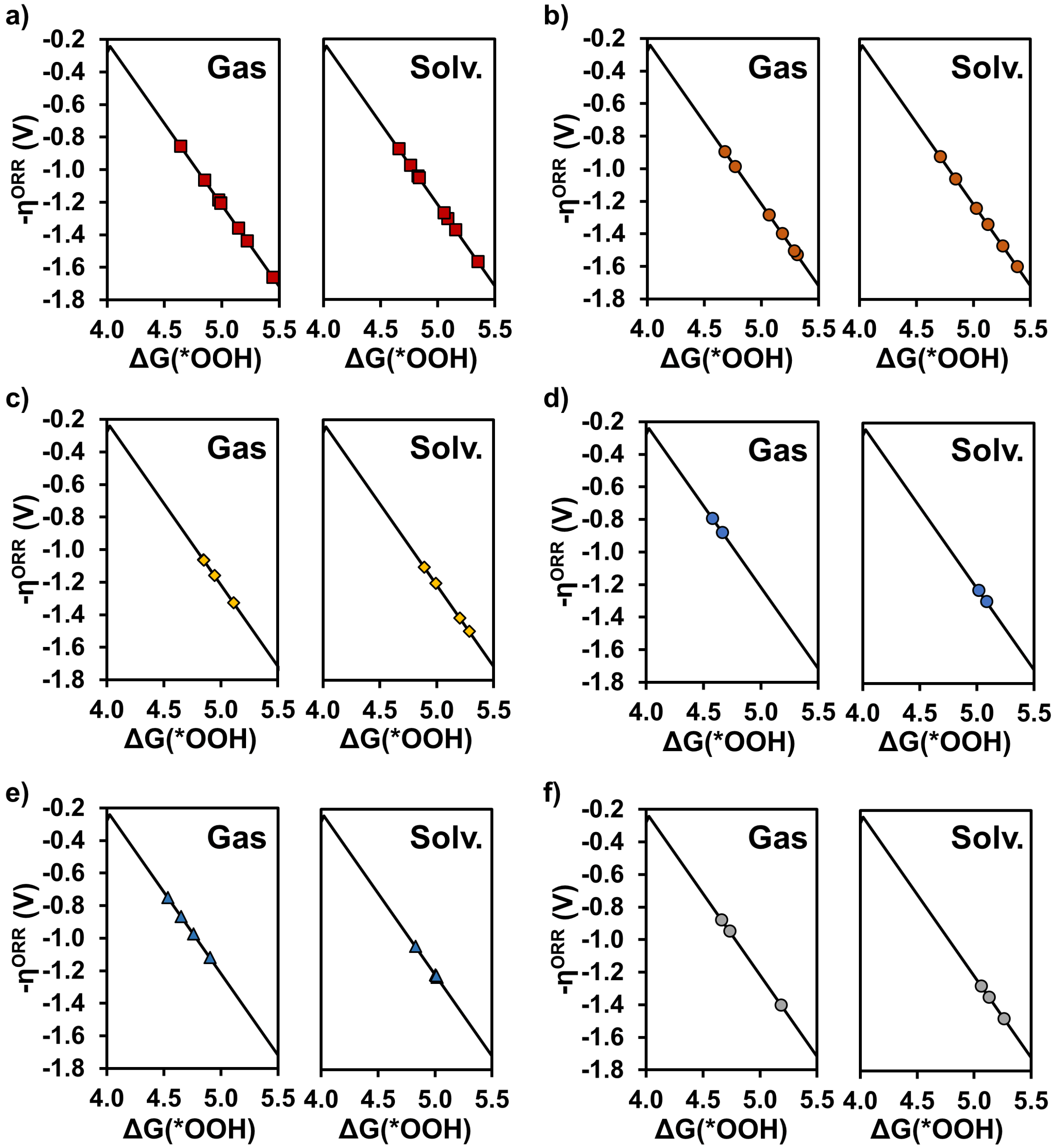

Figure S10: The ORR overpotentials for all potential reaction sites on the a) Amorphous, b) Defect B, c) Defect A, d) Swap B, e) Swap A, and f) Crystalline $TiAl_2O_5$ surfaces. All overpotentials are computed from PBE energies.

there is unaccounted for peak at 37.5 degrees which may correspond to an oxide film. Small amounts of additional secondary phases could still be present but below the detection limit

**Table S2: Determining the oxidation states of metal dopants by comparing Bader charges.**

| | **MO** | **$M_2O_3$** | **$MO_2$** | **$M_2O_5$** |
|---|---|---|---|---|
| Co | 1.21 | - | 1.38 | - |
| Cr | 1.39 | 1.60 | 1.77 | - |
| Ga | - | 1.58 | - | - |
| Mn | 1.29 | 1.48 | 1.58 | - |
| Nb | 1.36 | - | 2.30 | 2.67 |
| Si | - | - | 3.22 | - |
| Sn | 1.10 | - | 2.34 | - |
| | **Crystalline Surface** | | **Modified Crystalline Surface** | |
| | **Charge** | **Ox. State** | **Charge** | **Ox. State** |
| Co | 1.50 | 4+ | 1.09 | 2+ |
| Cr | 1.60 | 3+ | - | - |
| Ga | 1.70 | 3+ | - | - |
| Mn | 1.65 | 4+ | 1.31 | 2+ |
| Nb | 2.64 | 5+ | - | - |
| Si | 3.08 | 4+ | - | - |
| Sn | 2.16 | 4+ | - | - |
| | **Amorphous Surface** | | **Modified Amorphous Surface** | |
| | **Charge** | **Ox State.** | **Charge** | **Ox. State** |
| Co | 1.54 | 4+ | 1.09 | 2+ |
| Cr | 1.72 | 3+ | - | - |
| Ga | 1.66 | 3+ | - | - |
| Mn | 1.68 | 4+ | 1.36 | 2+ |
| Nb | 2.64 | 5+ | - | - |
| Si | 3.15 | 4+ | - | - |
| Sn | 2.18 | 4+ | - | - |

of the instrument. The solubility of silicon in alpha titanium is 0.3-0.5 wt%,[4] so a small amount of a secondary phase could be present. Aluminum dissolved into a titanium matrix contracts the lattice shifting the diffraction peaks to higher values of 2-theta, matching the shift of each cast TiAl alloy relative to cast Ti. In all cases, the TiAl alloys exhibited significant texture differences and likely had relatively large grains which would account for the presence of split peaks.

**Table S3: Al and Dopant Concentrations**

| **Alloy** | **Al Concentration in Oxide (at%)** | **Dopant Concentration in Oxide (at%)** |
|---|---|---|
| **TiAl** | 12.7 | - |
| **TiAl-Ga** | 13.2 | 2.5 |
| **TiAl-Si** | 9.9 | 1.3 |
| **TiAl-Sn** | 12.4 | 1.1 |

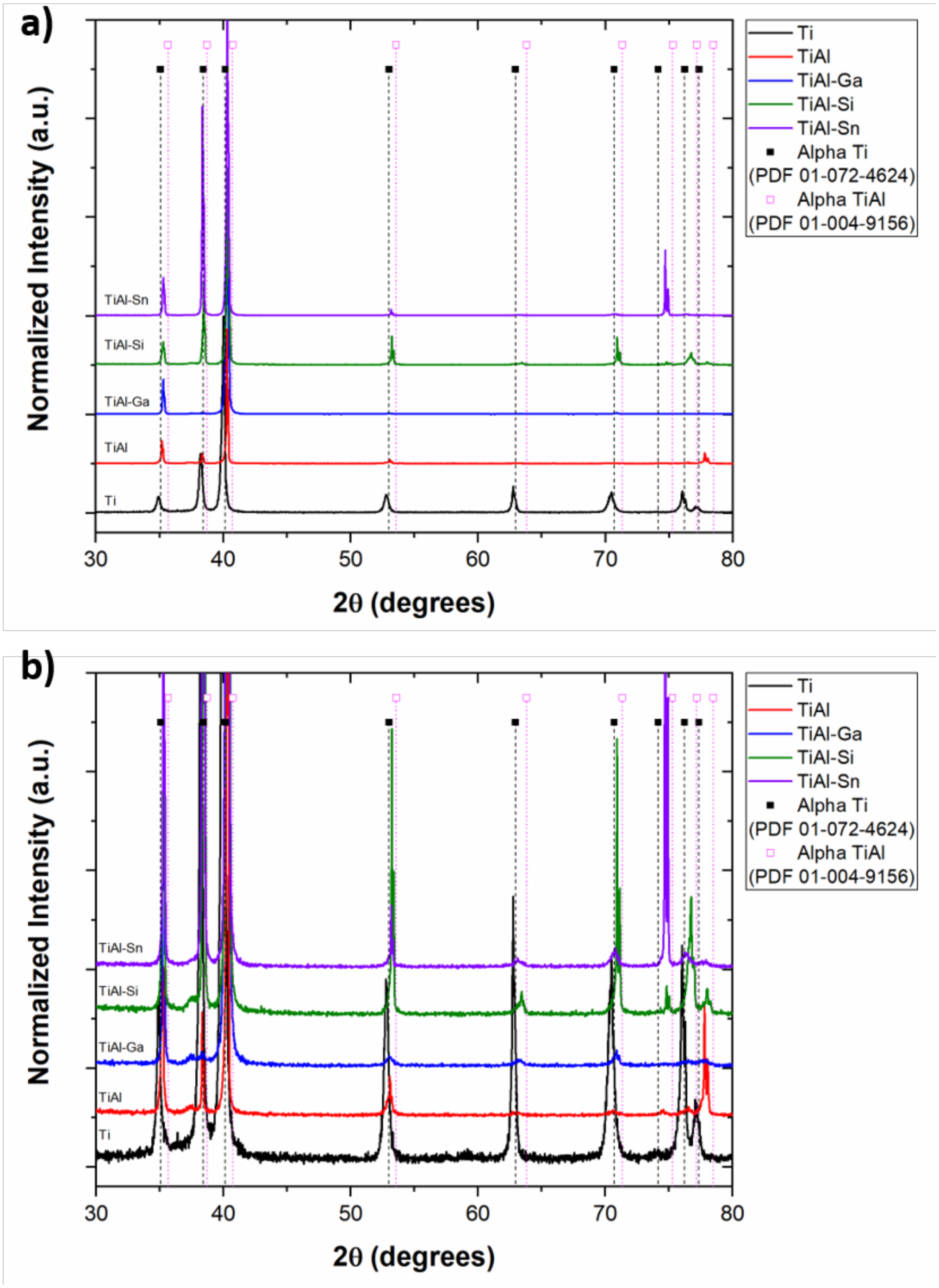

Figure S11: a) and b) X-ray diffraction spectra for each of the cast alloys as compared to pure titanium and an alpha TiAl standard.

# References

(1) Russo, M. Titanium oxide hydrates: Optical properties and applications. Ph.D. thesis, 2009.

(2) Ewing, C. S.; Bhavsar, S.; Veser, G.; McCarthy, J. J.; Johnson, J. K. Accurate amorphous silica surface models from first-principles thermodynamics of surface dehydroxylation. *Langmuir* **2014**, *30*, 5133–5141.

(3) Boes, J. R.; Groenenboom, M. C.; Keith, J. A.; Kitchin, J. R. Neural network and ReaxFF comparison for Au properties. *Int. J. Quantum Chem.* **2016**, *116*, 979–987.

(4) Luzhnikov, L. P.; Novikova, V. M.; Mareev, A. P. Solubility of $\beta$-stabilizers in $\alpha$-titanium. *Met. Sci. Heat Treat.* **1963**, *5*, 78–81.